



Published in final edited form as:

J Magn Reson Imaging. 2017 August ; 46(2): 323–337. doi:10.1002/jmri.25647.

MRI Assessment of Bone Structure and Microarchitecture

Gregory Chang, M.D., Sean Boone, B.S., Dimitri Martel, Ph.D., Chamith S. Rajapakse, Ph.D.², Robert S. Hallyburton, Mitch Valko, Stephen Honig, M.D.³, and Ravinder R. Regatte, Ph.D.

Department of Radiology, Center for Biomedical Imaging, NYU Langone Medical Center, 660 First Avenue, Room 334, New York, NY 10016

²Department of Radiology, Hospital of the University of Pennsylvania, 3400 Spruce Street, Philadelphia, PA 19104

³Osteoporosis Center, Hospital for Joint Diseases, NYU Langone Medical Center, 301 E. 17th Street, Suite 1101, New York, NY 10003

Abstract

Osteoporosis is a disease of weak bone and increased fracture risk caused by low bone mass and microarchitectural deterioration of bone tissue. The standard-of-care test used to diagnose osteoporosis, dual-energy x-ray absorptiometry (DXA) estimation of areal bone mineral density (BMD), has limitations as a tool to identify patients at risk for fracture and as a tool to monitor therapy response. Magnetic resonance imaging (MRI) assessment of bone structure and microarchitecture has been proposed as another method to assess bone quality and fracture risk in vivo. MRI is advantageous because it is noninvasive, does not require ionizing radiation and can evaluate both cortical and trabecular bone. In this review article, we summarize and discuss research progress on MRI of bone structure and microarchitecture over the last decade, focusing on in vivo translational studies. Single center, in vivo studies have provided some evidence for the added value of MRI as a biomarker of fracture risk or treatment response. Larger, prospective, multicenter studies are needed in the future to validate the results of these initial translational studies.

Keywords

Dual-energy x-ray absorptiometry (DXA); bone mineral density (BMD); bone quality; osteoporosis; finite element analysis (FEA); Fragility fractures

Introduction

Osteoporosis is a disease of weak bone and increased fracture risk caused by low bone mass and microarchitectural deterioration of bone tissue (1). Worldwide, 200 million people are affected by osteoporosis (2). In the U.S., 2 million fragility fractures occur annually, resulting in greater than \$17 billion in direct annual costs for fracture care (3). Fragility fractures can have severe morbidity and mortality. In women over age 45, osteoporosis

accounts for more days spent in the hospital than diabetes, myocardial infarction, and breast cancer (4), and in the first year after hip fracture, the mortality rate is as high as 20–24% (5, 6).

Osteoporosis is diagnosed by the occurrence of fragility fracture or by dual-energy x-ray absorptiometry (DXA) estimation of areal bone mineral density (BMD) in the hip or spine (7). For DXA, if a patient's BMD T-score is less than -2.5 (i.e., more than 2.5 standard deviations below the mean BMD for a population of 30 year old individuals of the same gender and race), then this patient is diagnosed as having osteoporosis. There is a strong association between low areal BMD and increased risk of fracture. One meta-analysis has shown that the predictive ability for a one standard deviation decrease in BMD is roughly similar to that of a one standard deviation increase in serum cholesterol concentration for prediction of cardiovascular disease (8).

However, DXA assessment of BMD has limitations. First, the majority of individuals who suffer fragility fractures do not have BMD T-scores < -2.5 and are misclassified as not having osteoporosis (9, 10). Indeed, the same meta-analysis mentioned above also concluded that BMD measurements cannot identify individuals who will have a fracture (8). This means that even if these individuals had received a DXA before suffering a fracture, they would not have been treated with a bone-strengthening drug, which can reduce fracture risk by ~50% (11).

Because of the low sensitivity of DXA, FRAX was developed. FRAX is a risk calculator that computes the 10-year probability of hip or major osteoporotic fracture by incorporating DXA-computed femoral neck areal BMD and clinical variables (age, gender, weight, height, fracture history, parental fracture history, alcohol and smoking history, glucocorticoid use, history of rheumatoid arthritis or secondary osteoporosis) (12). However, FRAX too has limitations and incompletely captures fracture risk (13). To improve fracture risk assessment, the trabecular bone score (TBS), an index of microarchitecture derived from a gray-scale texture analysis of DXA images, was developed and can be used to adjust an individual's FRAX score (14, 15). However, its correlation with microarchitecture in vivo and bone strength has been questioned (16, 17), and it can only be obtained in the lumbar spine, subject to the technical 2-D limitations of DXA (17).

Finally, monitoring response to osteoporosis therapy with DXA has shortcomings. BMD changes very slowly after the start of therapy, requiring two years to change 0–4% (18). The small magnitude of these changes makes dose-response studies challenging, and there is controversy over whether such small changes in BMD explain the antifracture effects of osteoporosis drugs (18).

The need for additional tools to diagnose osteoporosis, assess fracture risk, and monitor response to osteoporosis therapy have motivated the search for other methods to quantitatively assess and monitor bone fragility in vivo. Bone microarchitecture is an important contributor to bone strength independent of BMD and its deterioration is included in disease definition of osteoporosis (1). This review will summarize advances over the last

decade in magnetic resonance imaging (MRI) of bone microarchitecture, focusing on in vivo translational studies.

Bone Tissue

Bone tissue consists of approximately 65% inorganic matrix (minerals, mostly calcium hydroxyapatite crystals), which provides tissue stiffness, and 35% organic matrix (type I collagen, proteoglycans, bound water) which provides tissue tensile strength (19, 20). There are two types of bone tissue, trabecular bone and cortical bone.

Trabecular or cancellous bone is the internal compartment of bone tissue that consists by volume of approximately 25% bone and 75% marrow (Figure 1). On the microstructural level, trabecular bone consists of a complex 3-dimensional (3-D) network of trabecular plates and rods – its microarchitecture -- which helps provide tissue resistance to loading forces. Bone microarchitecture is an important contributor to bone strength independent of bone mass (21), and in the setting of osteoporosis, bone microarchitecture deteriorates, contributing to bone fragility (22, 23). Indeed, it is for this reason that deterioration of bone microarchitecture is included in the disease definition of osteoporosis (1).

Cortical or compact bone refers to the dense outer shell of bone tissue, which is approximately 90% bone and 10% pore space by volume (Figure 1). Most of the pore space represents Haversian canals, which reside in the center of the osteon, and the remainder reflects osteocyte lacunae and canaliculi. This architecture is designed to resist bending, torsional and shear forces (20). Cortical porosity is an important contributor to bone fragility (24), and there is evidence that metrics of cortical porosity may help discriminate subjects with fragility fractures from those without fractures independent of BMD (25, 26).

Technical Advances Over the Last Decade

MRI of Trabecular Microarchitecture

MRI of bone microarchitecture was first described approximately two decades ago in the distal radius and calcaneus (27–29). MRI of trabecular microarchitecture actually refers to imaging of the marrow contents of the trabecular bone tissue compartment; hyperintense marrow signal provides contrast to trabecular plates and rods, which are hypointense on conventional MR images. The technical requirements (hardware, pulse sequences) to perform MRI of bone microarchitecture have previously been comprehensively described in a prior JMRI review published in 2007 (30). In brief, the main requirement to perform MRI of trabecular microarchitectures is signal-to-noise ratio (SNR). A minimum SNR of 10 is recommended (30), which can permit voxel sizes of 0.137–0.250 mm and slice thicknesses of 0.4–1.5 mm in scan times of approximately 10–15 minutes. Since voxel size is directly proportional to SNR, decreasing both in-plane dimensions by approximately 30% will result in a 50% reduction in SNR. Superficial anatomic sites, such as the distal radius (0–2 cm from the skin surface), provide higher SNR than deeper anatomic sites, such as the hip (6–10 cm from the skin surface), due to their close proximity to the radiofrequency coil. As a result, for a given desired SNR, voxel sizes in the distal radius can be smaller than those that can be achieved in the hip. SNR gains can be facilitated by scanning at higher field strength

(31), using multichannel coils (with smaller coil dimensions) (32), and using SNR efficient pulse sequences (30, 33). The choice of scanner field strength, coil, and pulse sequence to use should also be balanced against the commercial availability of the hardware and software and the desired study goal. For example, 1.5T and 3T MRI scanners are currently more widely accessible than 7T MRI scanners, and therefore would currently be better choices for multicenter clinical studies. Peripheral extremity MRI scanners, though capable of imaging only the knee, wrist, or ankle, could also provide another means for widespread clinical use given their smaller physical footprint and lower cost. In contrast, for a single site research study focused on examining a disease or drug mechanism, a 7T MRI scanner using an in-house designed coil and pulse sequence that provide the highest possible SNR may be appropriate. Table 1 summarizing different techniques available for assessment of bone microarchitecture and structure

Over the last decade, given the increasing availability of high-field and ultra high-field MRI scanners, there have been a greater number of osteoporosis MRI studies performed at 3T and 7T. The increased signal-to-noise ratio (SNR) provided by higher field strength scanners can allow reductions in voxel size and scan times and can permit the scanning of more proximal skeletal sites, which because of their deeper anatomic location (resulting in lower SNR) are more challenging to image with same quality and resolution. While the early MRI studies of bone microarchitecture were performed in the distal extremities (wrist, ankle) (27, 28, 34), over the last decade, more proximal anatomic sites have been investigated including the proximal tibia, distal femur, and the hip or proximal femur (35–41). The ability to assess more proximal anatomic sites is important. Even though osteoporosis is a systemic disease, there is variation in bone quality and fracture susceptibility between the peripheral/central skeleton. For example, low hip BMD has a stronger association with hip fracture than low lumbar spine BMD (42). In addition, the correlation between microarchitectural parameters measured at peripheral versus central skeletal sites appears to be only modest or moderate ($r = 0.276$ to 0.522 in (43), $r = 0.34$ to 0.75 in (44), $r = 0.13$ to 0.56 in (45)).

Image Post-Processing for MRI of Trabecular Microarchitecture

Image processing for quantitative assessment of morphological and topological parameters of trabecular microarchitecture has also been previously described in great detail (30, 46–48). In general these methods aim to characterize the number, thickness, separation, connectivity, anisotropy, and shape of the trabecular struts that compose the trabecular bone microarchitectural network, with the goal of providing metrics similar to those obtained by histomorphometry.

One notable image processing advancement has been the application of finite element analysis (FEA) to MR images of bone microarchitecture (49–55). FEA is a mechanical engineering method that allows virtual stress testing of bones to compute metrics of bone mechanical competence (Figure 2). FEA has also been applied extensively in vivo to computed tomography (CT) (56–59) and high-resolution peripheral quantitative computed tomography (HR-pQCT) (51, 60–63) images of bone.

Ultrashort Echo Time MRI of Cortical Bone

Cortical bone is an important contributor to bone strength. Over the last decade, technical improvements in MRI have made it possible to assess and visualize tissues, such as cortical bone, that have very short T2 relaxation times (< 1 ms). This is accomplished by data acquisition using a very short or ultrashort echo time (UTE). The proton signal intensity in cortical bone is derived from: 1) cortical pore water (CPW) or water residing in microscopic pores, including Haversian canals and lacunae-canalicular systems ($T_2 > 1$ ms); 2) collagen-bound water (CBW) or water with restricted mobility bound to collagen within the bone matrix collagen ($T_2 = 0.3 - 0.4$ ms); and 3) protons of the collagen backbone or sidechain as well as of other species ($T_2 < 0.1$ ms) (64). A recent study provides evidence that signal from the latter proton species is not detectable with UTE MRI and that the UTE signal appears to be solely due to CPW and CBW (65). There are excellent recent reviews on UTE of cortical bone (66–68). These reviews describe in detail the data acquisition methods as well as summarize the experimental validation of UTE in specimen studies. Here, we focus on summarizing studies performed over the last decade in which UTE of cortical bone was applied in vivo to assess its potential as a biomarker of bone fragility.

Techawiboonwong et al reported one of the earliest applications of UTE on a clinical 3T scanner in vivo (69). Using a water phantom placed at the anterior aspect of the subject's tibia and a UTE sequence ($TR = 70$ ms, $TE = 70$ us) without soft tissue signal suppression, the authors determined total bone water (BW) concentration (sum of CBW and CPW) as a ratio of signal intensities of the reference and bone. They applied this method in three different groups of patients: postmenopausal females (age = 34.6 ± 5.3 years, $n=5$), premenopausal females (age = 69.4 ± 6.6 years, $n=5$), and patients with renal osteodystrophy (age = 51.8 ± 6.5 years, $n=6$). The authors found that renal osteodystrophy subjects had 135% higher BW than pre-menopausal subjects ($p < 0.001$) and 43% higher BW than post-menopausal subjects ($p = 0.02$). Of note, there was only a 6% difference in tibial volumetric BMD between the pre- and post-menopausal subjects ($p < 0.003$) and no difference in volumetric BMD between the renal osteodystrophy subjects and the control subjects of any age. Since subjects with renal osteodystrophy have increased fracture risk, the results suggested that cortical bone water may provide additional useful information beyond BMD for assessment of bone fragility.

Because BW arises from two contributions (CPW and CBW), which may be disproportionately affected in aging or in the setting of disease, investigators have proposed methods to discriminate between these two water contributions. Again, we focus on in vivo studies. Manhard et al. used a double adiabatic full passage (DAFP) sequence and an adiabatic inversion recovery (AIR) sequence to scan five healthy subjects (two males, three females, ages = 24–49 years) three times each at the distal radius and distal tibia at 3T (70). The DAFP sequence suppresses CBW while maintaining CPW signal, and the AIR sequence selectively nulls CPW while retaining CBW signal. Scan times were 14 minutes each for AIR and DAFP in the tibia. Using an external phantom scanned with the subjects, the authors calculated aggregate mean (across all scans) tibial bound water and pore water concentrations of 27.86 ± 2.00 moles per liter and 7.32 ± 1.15 moles per liter, respectively.

This study importantly assesses measurement reproducibility of UTE of cortical bone in vivo, which is necessary for any test being translated to clinical use.

Chen et al. recently used 3-D UTE imaging with a radial cones trajectory to image the tibial midshaft of six male volunteers (age = 34.6 ± 6.8 years) at 3T (71). They performed: 1) 3-D UTE with interrelated dual echoes (FOV = 15 cm, matrix = 192×192 , slice thickness = 10 mm, number of slices = 10, scan time = 1.8 minutes) and bicomponent analysis to quantify both CBW and CPW values and 2) 3-D UTE-IR (FOV = 15 cm, matrix = 128×128 , slice thickness = 10 mm, number of slices = 10, scan time = 2.0 minutes) to quantify CBW by suppressing CPW signal. Overall, the calculated in vivo percentages of CBW ($68.8 \pm 6.1\%$) and CPW ($31.2 \pm 6.1\%$) by the bicomponent analysis were in agreement with prior studies, and single component decay was observed with the 3-D IR-UTE sequence consistent with CPW being nulled and CBW water being selectively detected in vivo.

Li et al. developed a 2-D UTE-derived metric termed the suppression ratio (SR) as biomarker of cortical porosity (72). Unlike biexponential analysis, which requires multiple time points, the SR method requires only two points and was calculated as the ratio of unsuppressed UTE signal to the long T2 suppressed UTE signal. Two long-T2 suppression methods were tested in vivo including a dual-band saturation-prepared UTE sequence and an adiabatic inversion recovery UTE sequence, and the correlation between the two methods was high ($r = 0.98$, $p < 0.001$). In seven subjects scanned two times at the mid-tibia at 3T, the authors found the reproducibility of the suppression ratio method to be high with an average within-subjects coefficient of variation of 1.5% using the IR technique. Finally, in 40 female subjects with an age range of 20 to 80 years, the authors found that the SR had a stronger correlation with age ($r = 0.64$, $p < 0.001$) than total BW ($r = 0.52$, $p = 0.002$), suggesting that SR may have added value, beyond total BW, as a biomarker of bone fragility with aging.

More recently, Rajapaske et al., described the specimen validation and clinical application of a method to map volumetric cortical bone porosity (the porosity index) calculated from the ratio of UTE signal intensity obtained at a long echo time to the signal intensity obtained at a short echo time (TR 12 msec, TE = 50 μ sec/4600 μ sec, FOV = 16 cm \times 16 cm \times 16 cm, $320 \times 320 \times 320$ matrix, scan time < 10 minutes) (73). An in vivo reproducibility study of 5 subjects (two women, three men, age range = 26 – 41 years) demonstrated mean coefficients of variation for cortical and total bone porosity of 2.2% and 2.0%, respectively. Furthermore, the authors showed that they could capture pore size information (as validated by microcomputed tomography) and demonstrated that they could detect in vivo a range of porosity indices (15%–31% and 24%–38% for cortical and total bone regions) in 34 post-menopausal women (age range = 55–80 years) (Figure 3).

In summary, UTE MRI is a promising method that provides quantitative information about cortical bone porosity and collagen-bound water. Because of the relative novelty of the method, there are few in vivo clinical studies to date. In vivo clinical translation will be facilitated by improvements in hardware (fast transmit-receive switches, high performance gradients), which will increase SNR and improve image quality, and the development and standardization of UTE product sequences and data processing software across vendors.

This will permit researchers and clinicians to determine the best data acquisition schemes. For example, while data processing methods like bicompartamental T2* mapping is easily available, there may be variation in results secondary to the choice of echo times, the SNR, and the relaxation model which may not fully describe the entire UTE signal (74). IR methods do not require multiple echoes or as high of an SNR as biexponential analysis, but signal variation from B1+ field inhomogeneity could affect results. The suppression ratio and porosity index are methods which may help overcome some of these limitations. Finally, we note that other solid state MRI methods for evaluating cortical bone have been described including zero echo time (ZTE) MRI (75, 76), sweep imaging with Fourier transform (77), which has been applied in teeth in vivo (78), and 31P MRI (76, 79), which has also been performed in vivo (80, 81), and would permit the eventual in vivo evaluation of bone mineral density using MRI.

Assessment of Bone Physiology

Although this review focuses on the advancements on in vivo MRI of bone microarchitecture and structure over the last decade, we do note that important progress has also been made on using MRI as a tool to evaluate bone physiology. In particular, there has been increasing literature on the use of MRI to quantitatively assess marrow fat content and composition using spectroscopy and chemical shift-based methods (82–92). The development of such methods is important because marrow fat may serve as a risk factor for osteoporosis independent of bone mineral density (93). Additional studies have investigated the use of perfusion MRI (94–101) and diffusion MRI (102–108) as methods to assess bone vascularity and marrow cellularity as risk factors for osteoporosis. Finally, with the recent arrival of positron emission tomography (PET)/MRI scanners, it is now possible to assess bone turnover and metabolism in combination with anatomic imaging. Previously PET has demonstrated potential as method to assess metabolic activity and bone formation in patients with osteoporosis, including individuals on therapy (109–112).

MRI of Bone Microarchitecture for Assessment of Fracture Risk and Monitoring of Disease Progression

Reproducibility Studies

Reproducibility studies are important, because these will allow clinicians and researchers in the future to determine sample sizes for large clinical studies aimed at predicting fracture or monitoring therapy response. In the early 2000s, Newitt et al. (113) and Gomberg et al. (114) demonstrated the coefficients of variation for MRI assessment of bone microarchitecture to range from 3.4–8.3% within the distal radius (113) and from 4–7% within the distal radius and tibia (114), respectively. Within the last decade, several additional reproducibility studies have been performed at 1.5T, 3T, and 7T.

Carballido et al. scanned six subjects in vivo (2 scans, 5 minutes apart with repositioning between scans,) at the distal radius and distal tibia at 1.5T (3D-GRE sequence, 0.156 mm × 0.156 mm × 0.5 mm). Reported coefficients of variation (CVs) for quantitative assessment of morphological and topological microarchitectural parameters ranged from 1.01% to 8.3%

in the distal radius and 0.99% to 7.70% in the distal tibia, with an overall average reproducibility of 4.8%.

Lam et al. scanned 20 subjects in vivo (3 scans over the course of 8 weeks) at the distal radius at 1.5T (3-D FLASE, 0.137 mm × 0.137 mm × 0.410 mm) and reported similar results on a different scanner and using a different image processing algorithm (115). For whole section trabecular regions of interest, they reported aggregate mean CVs/intraclass correlation coefficients (ICCs) of 4.4%/0.946 and 4.0%/0.974 for microstructural parameters and axial bone stiffness, respectively. For subregional trabecular regions of interest, corresponding values were 6.5%/0.946 and 5.5%/0.974 for microstructural parameters and mechanical parameters, respectively.

Wald et al. investigated the reproducibility for quantitative assessment of microarchitectural and mechanical parameters within the distal tibia at 3T and at two resolutions (7 subjects, 3 scans over 6 months, 3-D FLASE, 0.137 mm × 0.137 mm × 0.410 mm and 0.160 mm × 0.160 mm × 0.160 mm) (116). The anisotropic data demonstrated in general better reproducibility with CVs/ICCs for microarchitectural and mechanical parameters ranging from 1.0%–5.2%/0.75–0.99. For isotropic data, the CVs/ICCs for microarchitectural and mechanical parameters ranged from 0.87%–8.1%/0.62–0.99.

Zuo et al. scanned six subjects in vivo (two times with repositioning between scans) at the knee at 7T (3-D SSFP, 10 cm FOV, 512 × 384 matrix, 1 mm slice thickness) and demonstrated CVs of 1.07%–3.30% for trabecular microarchitectural parameters in the distal femur (117). Similar results were obtained by Bhagat et al., who scanned 5 subjects in vivo (3 scans over the course of 3 months) at the distal tibia at 7T (3-D FSE, 0.137 mm × 0.137 mm × 0.410 mm) (118). For whole and subregional analyses, the CVs/ICCs ranged from 1.5%–4.41%/0.95–0.99 and 1.22%–4.77%/0.96–0.99 for microarchitectural parameters and mechanical parameters, respectively.

More recently, Hotca et al. and Chang et al. investigated the reproducibility of quantitative assessment of microarchitectural and mechanical parameters (computed with linear FEA) in the proximal femur at 3T (11–12 subjects, 3 scans, twice on one day and once one week later, 3-D FLASH, 0.234 mm × 0.234 mm × 1.5 mm) (119, 120). For microarchitectural parameters, within-day root-mean-square CVs/ICCs ranged from 2.3%–7.8%/0.931–0.989 and between-day root mean square CVs/ICC ranged from 4.0%–7.3%/0.934–0.971. For mechanical parameters, within and between day root mean square CVs/ICCs ranged from 3.5%–6.6%/0.96–0.98.

Finally, Rajapakse et al. showed that it is now possible to assess MRI-based strength measures at the level of the whole proximal femur with high reproducibility in vivo using nonlinear FEA (121). Median CVs/ICCs for the several parameters computed including yield strain, yield load, ultimate strain, ultimate load, resilience and toughness were < 8% with ICCs of 0.99.

Overall, the reported CVs/ICCs are within a range suitable for clinical studies of disease detection or monitoring of disease progression/treatment response. Because scan times are relatively long (> 10 minutes), minimizing patient motion (by immobilizing the scanned

body part) as well as the application of prospective and retrospective registration techniques can improve reproducibility.

Post-Menopausal Osteoporosis

Post-menopausal women are the largest population affected by osteoporosis and not surprisingly have been the most commonly evaluated cohort in MRI studies of bone microarchitecture. In one 3T MRI study of the hip (3-D FLASH, 0.234 mm × 0.234 mm × 1.5 mm), 22 post-menopausal women with fragility fractures were compared to 22 age, gender, and BMI-matched controls without fracture (Figure 4). Finite element analysis was applied to images of proximal femur microarchitecture to compute elastic moduli in five subregions of the proximal femur. Subjects with fragility fracture demonstrated lower MRI-computed elastic moduli (−33.2% to −66.8% of control values, $p = 0.04$ – 0.006) in all regions of the proximal femur compared to the controls (40). In contrast, there were no differences in femoral neck, total hip, or spine BMD T-scores between groups. Overall, the results suggest that MRI of bone microarchitecture and strength may have value beyond that of BMD for fracture risk assessment.

In another study of the distal radius at 1.5T (3-D FLASE, 0.137 mm × 0.137 mm × 0.400 mm), 18 post-menopausal women with a history of low-energy fracture were compared to 18 age, race, and BMD-matched post-menopausal women without fracture (122). All women in this study were not osteoporotic by densitometric criterion (i.e. had BMD T-scores > −2.5). Fracture subjects had 14% lower surface-curve ratio (marker of trabecular plate-to-rod ratio, $p = 0.04$), 17% higher erosion index (marker of trabecular network resorption, $p = 0.03$), and 9% lower trabecular bone volume fraction ($p < 0.001$) compared to controls. There were no differences in hip, spine, or distal radius BMD between groups. Of note because all subjects were classified by DXA as not osteoporotic, the results suggest that MRI might have the potential to detect individuals at increased fracture risk who are not detectable by standard DXA criteria.

In another study of the distal femur at 7T (3-D FLASH, 0.234 mm × 0.234 mm × 1 mm), 31 post-menopausal females with fragility fracture were compared to 25 post-menopausal control subjects without fracture (123). Subjects with fragility fracture demonstrated deterioration in several microarchitectural parameters compared to controls, and in particular 450% higher trabecular isolation and 341% higher trabecular rod-like structure ($p < 0.03$ for all) while differences in hip and spine DXA T-scores between groups were not significant ($p > 0.05$) (Figure 5). In addition, in ROC analyses, microarchitectural parameters could discriminate fracture cases from controls (AUC = 0.66–0.73, $p < 0.05$), while hip and spine BMD T-scores could not (AUC = 0.58–0.64, $p > 0.07$). Limitations of this study include the limited availability of 7T MRI scanners, and near-significant differences in BMD T-scores between groups.

Finally, ninety-six women with hip or spine t-scores between −1.5 and −3.5 underwent 1.5T MRI of the distal tibia and distal radius (3-D FLASE, 0.137 mm × 0.137 mm × 0.410 mm) and had their spinal deformity index measured on midline sagittal MRI (124). The combination of distal radial trabecular surface density and trabecular bone volume fraction were found to account for 30% of the variation of spinal deformity index ($r^2 = 0.31$, $p <$

0.0001) independent of spinal BMD, which demonstrated no significant correlation with spinal deformity ($r = 0.16$, $p = 0.09$). This cohort was later analyzed using finite element analysis to estimate stiffness in the distal tibia and distal radius (125). Total tibial stiffness correlated with biconcave fractures ($r = 0.67$, $p < 0.005$), wedge fractures ($r = 0.57$, $p < 0.005$), but not crush fractures ($r = 0.27$, $p > 0.05$). With the exception of the total radial stiffness and biconcave fractures ($r = 0.40$, $p < 0.05$), radial measures were not correlated with fracture type ($r = 0.07$ – 0.32 , $p > 0.05$).

Males on Antiandrogen Therapy

By preventing androgen synthesis, antiandrogen therapy for prostate cancer puts men at higher risk for fragility fracture. In one study, 137 older men treated with greater than 6 months of androgen deprivation therapy were scanned with clinical DXA to assess BMD and with 1.5T MRI of the right forearm to assess microarchitecture (126). Screening vertebral fracture assessment revealed fractures in 51 men, the majority of which had not been previously diagnosed. Men with moderate to severe vertebral fractures demonstrated deterioration in distal radius microarchitecture compared to controls without fracture, including lower bone volume fraction (-15% , $p < 0.05$), lower surface density (-19% , $p < 0.05$), and higher erosion index ($+22\%$, $p < 0.05$). In ROC analyses, the addition of MRI parameters to BMD resulted in statistically significant improvements in the ability to discriminate fracture cases from controls (AUC for hip and spine T-scores = 0.804, AUC for hip and spine T-scores and MRI measures = 0.89; $p = 0.040$ for increase in AUC).

Glucocorticoid-Induced Osteoporosis and Renal Osteodystrophy

Glucocorticoid-induced osteoporosis is the most common secondary form of osteoporosis (127). However, there is no clear relationship between BMD and fracture risk in long-term glucocorticoid users (128). In one small 3T MRI study of the hip (3-D FLASH $0.234 \text{ mm} \times 0.234 \text{ mm} \times 1.5 \text{ mm}$), six subjects (2 male, 4 female) with > 1 year cumulative glucocorticoid use were compared to six healthy controls (2 male 4 female) (129). The controls were older than the glucocorticoid users and the glucocorticoid users had higher median hip BMD T-scores compared to controls (femoral neck -2.1 vs -2.6 , $p = 0.24$, total hip -1.3 vs -2.3 , $p = 0.002$). However, despite this, compared to the controls, the glucocorticoid users had lower femoral neck trabecular number (-50.3% , $p = 0.02$), trabecular plate-to-rod ratio (-20.1% , $p = 0.03$), higher trabecular separation ($+191\%$, $p = 0.02$), and lower elastic modulus (-64.8 to -74.8% , $p < 0.05$). The study is limited by a small sample size, but highlights the possible utility of MRI of microarchitecture, beyond simply BMD assessment, for the diagnosis of osteoporosis and assessment of fracture risk in long-term glucocorticoid users.

In a 1.5T MRI study of the distal tibia (3-D FLASE, $0.137 \text{ mm} \times 0.137 \text{ mm} \times 0.410 \text{ mm}$), 49 patients (24 female, 25 male) were evaluated at 2 weeks and 6 months after renal transplantation (130). The post transplant regimen included glucocorticoids for all participants. Participants had a small yet significant decrease in spine BMD ($< 3\%$, $p < 0.0001$) and no change in hip BMD. Compared to baseline, multiple measures of bone strength as computed by FEA decreased over time, including cortical stiffness (-3.72% , $p = 0.03$), cortical failure strength (-7.61% , $p = 0.0003$), trabecular stiffness (-4.94% , $p = 0.03$)

and failure strength (-5.95% , $p = 0.004$), whole bone stiffness (-4.29% , $p = 0.003$) and failure strength (-5.61% , $p = 0.0004$). Trabecular number, thickness, and bone volume fraction did not show any significant changes over 6 months, raising the possibility that MR estimates of bone strength might provide additional sensitivity for monitoring longitudinal changes compared to microarchitectural measures themselves.

Diabetes

Subjects with type I diabetes and type II diabetes are at increased risk for fracture (131, 132). In a 3T MR study of the proximal tibia ($0.3 \text{ mm} \times 0.3 \text{ mm} \times 0.3 \text{ mm}$), 30 young women with type 1 diabetes were compared to 28 healthy female controls (133). Compared to controls, diabetic subjects demonstrated reduced apparent bone volume fraction (-9.1% , $p = 0.018$), reduced trabecular number (-10% , $p = 0.012$), higher trabecular separation ($+12\%$, $p = 0.012$). Diabetic subjects also demonstrated significant difference in multiple MRI measures of subcutaneous, visceral and total body tissue adiposity.

In a 1.0 T MRI study of the distal radius (3-D GRE, $0.195 \text{ mm} \times 0.195 \text{ mm} \times 1 \text{ mm}$), 30 postmenopausal women with Type 2 diabetes were compared to 30 postmenopausal female controls (134). There were no differences between groups in terms of bone volume fraction (-1% , $p = 0.45$), trabecular thickness (0% , $p = 0.59$), trabecular spacing (-1% , $p = 0.29$), trabecular number ($+2\%$, $p = 0.25$), or BMD T-scores ($p > 0.05$). Trabecular bone network hole size was, however, significantly increased in diabetic subjects compared to controls ($+13\%$, $p = 0.011$). In a two year follow-up study of approximately half of the original subjects (135), diabetic subjects demonstrated a greater percent change in number of trabecular bone holes compared to controls ($+10\%$ versus -7% , $p = 0.01$) after adjusting for ethnicity, but this result was no longer significant after adjusting for multiple comparisons ($p = 0.09$). The use of 1.0T, which has lower signal-to-noise ratio (SNR) compared to 1.5T, 3T, or 7T, may have contributed to the inability to detect longitudinal changes in this study.

Disuse Osteoporosis

In a 1.5T MRI study of the distal femur (3-D GRE, $0.175 \text{ mm} \times 0.175 \text{ mm} \times 0.700 \text{ mm}$), 10 children with disuse osteoporosis secondary to cerebral palsy were compared to 10 healthy age and gender matched controls (136). Compared to controls, patients with cerebral palsy demonstrated lower apparent bone volume (-30% , $p < 0.05$), lower trabecular number (-21% , $p < 0.05$), lower trabecular thickness (-12% , $p < 0.05$), and higher trabecular separation ($+48\%$, $p < 0.05$). Patients with cerebral palsy also demonstrated lower areal BMD compared to controls (-37% , $p < 0.05$). A subsequent study by the same authors involving 12 children with cerebral palsy and 12 controls recapitulated these findings, and microarchitectural deterioration worsened as the distance from the growth plate increased (137).

Future Work

The body of work above provides evidence that MRI can detect microarchitectural deterioration in patients with primary or secondary osteoporosis compared to controls and that there may be added value beyond BMD for assessment of fracture risk. These in vivo translational studies have been cross-sectional and have had relatively small sample sizes (<

100 subjects). In the future, it will be important to perform longitudinal studies with larger numbers of subjects to determine if microarchitectural parameters have benefit beyond BMD and/or FRAX for prediction of incident fracture. It will also be important to standardize the imaging method (skeletal location, field strength, pulse sequence, voxel size) and determine which microarchitectural parameter or combination of parameters should be measured to be assess fracture risk.

MRI of Bone Microarchitecture for Monitoring Treatment Response

There is increasing evidence that MRI can be used to monitor longitudinal changes in bone microarchitecture in response to bone-strengthening interventions.

Treatment Response: Postmenopausal Women

Greenspan et al. performed a 12 month longitudinal study of 10 post-menopausal women treated with risedronate using 1.5T MRI of the distal radius and DXA of the hip, spine, and distal radius (138). No control group was followed longitudinally. At 12 months, risedronate-treated subjects demonstrated a $13.0 \pm 5.4\%$ increase in surface-curve ratio (trabecular plate-to-rod ratio, $p < 0.05$) and a $12.1 \pm 3.1\%$ decrease in erosion index (inverse marker of trabecular network connectivity, $p < 0.01$) compared to baseline. No significant longitudinal changes in MRI-computed bone volume fraction or DXA-computed areal BMD at any location were identified, suggesting that monitoring microarchitectural parameters, might provide benefit for monitoring therapy response, beyond simply monitoring bone mass.

Folkesson et al. performed a longitudinal study of 53 post-menopausal osteopenic women who were randomized to either treatment with alendronate (70 mg weekly plus calcium and vitamin D, $n = 26$) or to a control group (calcium and vitamin D only, $n = 27$) (139). Compared to baseline, the alendronate group demonstrated statistically significant 24-month longitudinal changes in 3T MR-derived microarchitectural parameters in the distal tibia including higher BV/TV (+3.53%), higher trabecular number (+4.43%), lower trabecular separation (-5.35%), and decreases in inverse markers of trabecular connectivity (-2.69% to -3.52%). Areal BMD was monitored in the distal radius, and the difference in percent longitudinal change in areal BMD between the treatment group and control group was statistically significant at 12 (+1.84%) and 24 months (+2.66%).

Black et al. performed a 12 month longitudinal study of 50 osteopenic post-menopausal women who were randomized to either parathyroid hormone (PTH 1-84) therapy ($n = 25$) or placebo ($n = 25$) (140). Compared with the placebo group, PTH-treated women demonstrated increased lumbar spine areal BMD (+2.1%, $p = 0.03$) and MRI-computed distal radius trabecular bone volume, number, and thickness ($p = 0.04$). The latter microarchitectural changes were observed in the most proximal aspect of the distal radius only. Of note, there were no statistically significant changes in areal hip or femoral neck BMD or volumetric BMD at the hip or spine, suggesting that MRI might provide some additional benefit for monitoring treatment response.

Finally, Wehrli et al. performed a 24 month longitudinal study of 32 early menopausal women on estradiol therapy and 33 matched female controls using DXA and 1.5T MRI of the distal radius and tibia (141). Compared to baseline, at 12 months, there were no significant changes in microarchitectural parameters in the treatment group. However, the control group demonstrated deterioration in distal tibial trabecular microarchitecture manifested by 5.6% lower surface-curve ratio (marker of plate-rod ratio), $p < 0.0005$, 7.1% higher erosion index (marker of osteoclastic network resorption, $p < 0.0005$), and higher curve (9.8%) and profile (5.1%) edges (reflecting from disconnection of rod-like trabeculae, $p < 0.001$ for both). By 24 months, within the treatment group, microarchitectural parameters changed by as much as 10.81% (surface-interiors, $p = 0.03$) compared to baseline, while no statistically significant increases in areal hip or spine BMD were detected ($p = 0.52$). Furthermore, for microarchitectural parameters, differences in the mean changes from baseline between the treatment and control group were as high as 13% (surface-curve ratio, $p = 0.005$), while for spine and hip areal BMD differences in mean changes from baseline between the two groups was $< 5.0\%$ ($p < 0.005$). In a follow-up study, Wehrli et al. showed that the same treated subjects also demonstrated higher FEA-computed distal tibial axial stiffness at 12/24 months (5.8%/6.2%, $p < 0.05$), while the control subjects demonstrated decreased axial stiffness at the same time points (3.9%/4.0%, $p < 0.005$). Overall, the results suggest that monitoring of trabecular microarchitectural parameters may have added value beyond BMD as a sensitive means to monitor bone response to estradiol therapy.

Treatment Response: Hypogonadal Men

Zhang et al. performed a 24 month longitudinal study of 10 hypogonadal men treated with a testosterone gel and as 10 eugonadal male controls (142). The subjects received a 1.5T MRI of the distal tibia at baseline and after 6, 12, and 24 months of treatment. In hypogonadal men, at 24 months compared to baseline, there were statistically significant increases in the elastic moduli of a subvolume of the distal tibia (+9.0% for E_{22} , +5.1% for E_{33} , $p < 0.05$ for both) and significant increases in the standard morphological parameters of trabecular thickness (+2.0%, $p < 0.05$) and bone volume fraction (+3.4%, $p < 0.05$). In eugonadal men, at 24 months compared to baseline, there were no statistically significant changes in distal tibia elastic moduli or trabecular microarchitectural parameters.

Treatment Response: Spinal Cord Injury Patients

Gordon et al. performed a longitudinal study of 10 male and 2 female patients with disuse osteoporosis secondary to spinal cord injury (143). These patients were treated with physical therapy and teriparatide and had DXA and 3T MRI of the distal tibia at baseline, 3 months, and 6 months. Only six subjects completed the MRI at 3 months and only 4 subjects completed the MRI at 6 months. Compared to baseline, at 3 months the subjects demonstrated 23.6±22.3% higher surface-to-curve ratio, 17.04±12.9% lower erosion index, and 4.4±4.06%, greater trabecular thickness ($p < .05$ for all); however, these improvements in bone microarchitecture did not remain statistically significant at 6 months. MRI-computed bone volume fraction and DXA measurements of spine or hip BMD did not demonstrate any statistically significant differences compared to baseline at 3 or 6 months suggesting that

measurement of bone mass alone may not capture treatment changes. However, this study had a small sample size, 66% attrition, and lacked a control group.

Future Directions and Conclusion

In summary, over the last decade, advancements in MRI of bone microarchitecture and structure include the application of finite element analysis to MR images to compute metrics of bone strength, the initial in vivo translation of UTE methods to assess cortical bone porosity and collagen bound-water in vivo, the extension of MRI of microarchitecture to more proximal anatomic locations, including the hip, and the application of the MRI methods in a variety of patient populations (females, males, disuse osteoporosis, steroid therapy, renal osteodystrophy, diabetes) in cross-sectional studies to detect disease and longitudinal studies to monitor treatment response.

The majority of MRI studies have been performed at 1.5T and 3T scanners, which are widely available, and MRI does have the advantage of not requiring ionizing radiation and being able to assess trabecular and cortical bone microarchitecture. However, larger, prospective studies are needed to determine whether the MRI methods can predict future fracture or fracture risk reduction in response to therapy, and whether there is value in measuring these microarchitectural parameters beyond DXA-computed areal BMD.

It also remains to be determined whether the microarchitectural information obtained by MRI has benefit beyond other methods to assess fracture risk and monitor treatment response, including: FRAX; trabecular bone score (TBS), which is assumed to correlate with microarchitecture and derived from a texture analysis of DXA images (no additional imaging required, but can currently only be obtained in the lumbar spine and is subject to 2-D technical limitations of DXA); conventional computed tomography (can obtain BMD information and widely available, but lower resolution and requires ionizing radiation); and high-resolution peripheral quantitative computed tomography (higher resolution, but can be performed only in peripheral extremities and not widely available).

Finally, the cost-effectiveness of these methods should be determined. In the field of cardiology, risk stratification for ischemic heart disease involves clinical risk assessments (e.g. Framingham heart score), relatively simple laboratory and bedside testing (cholesterol, blood pressure, electrocardiogram (ECG)), and more advanced testing (exercise treadmill ECG testing, nuclear medicine, echocardiography), which collectively have improved the care of patients at risk for myocardial infarction. It will take time, but hopefully, the novel MRI tools being developed and tested in the field of osteoporosis will similarly improve the care of patients at risk for fragility fracture.

Acknowledgments

NIH Funding: R01-AR070131 (G.C.), R01-AR066008 (G.C.), R01-AR068382 (C.S.), R01-AR060238 (R.R.), R01-AR067156 (R.R.), R01-AR068966 (R.R.)

References

1. Consensus development conference: diagnosis, prophylaxis, and treatment of osteoporosis. *Am J Med.* 1993; 94(6):646–50. [PubMed: 8506892]
2. Johnell O, Kanis JA. An estimate of the worldwide prevalence and disability associated with osteoporotic fractures. *Osteoporos Int.* 2006; 17(12):1726–33. [PubMed: 16983459]
3. Burge R, Dawson-Hughes B, Solomon DH, Wong JB, King A, Tosteson A. Incidence and economic burden of osteoporosis-related fractures in the United States, 2005–2025. *J Bone Miner Res.* 2007; 22(3):465–75. [PubMed: 17144789]
4. Kanis JA, Delmas P, Burckhardt P, Cooper C, Torgerson D. Guidelines for diagnosis and management of osteoporosis. The European Foundation for Osteoporosis and Bone Disease. *Osteoporos Int.* 1997; 7(4):390–406. [PubMed: 9373575]
5. Leibson CL, Tosteson AN, Gabriel SE, Ransom JE, Melton LJ. Mortality, disability, and nursing home use for persons with and without hip fracture: a population-based study. *J Am Geriatr Soc.* 2002; 50(10):1644–50. [PubMed: 12366617]
6. Cooper C, Atkinson EJ, Jacobsen SJ, O'Fallon WM, Melton LJ 3rd. Population-based study of survival after osteoporotic fractures. *Am J Epidemiol.* 1993; 137(9):1001–5. [PubMed: 8317445]
7. Kanis JA. Diagnosis of osteoporosis and assessment of fracture risk. *Lancet.* 2002; 359(9321):1929–36. [PubMed: 12057569]
8. Marshall D, Johnell O, Wedel H. Meta-analysis of how well measures of bone mineral density predict occurrence of osteoporotic fractures. *BMJ.* 1996; 312(7041):1254–9. [PubMed: 8634613]
9. Wainwright SA, Marshall LM, Ensrud KE, et al. Hip fracture in women without osteoporosis. *J Clin Endocrinol Metab.* 2005; 90(5):2787–93. [PubMed: 15728213]
10. Schuit SC, van der Klift M, Weel AE, et al. Fracture incidence and association with bone mineral density in elderly men and women: the Rotterdam Study. *Bone.* 2004; 34(1):195–202. [PubMed: 14751578]
11. Miller PD, Derman RJ. What is the best balance of benefits and risks among anti-resorptive therapies for postmenopausal osteoporosis? *Osteoporos Int.* 2010; 21(11):1793–802. [PubMed: 20309524]
12. Kanis JA, Johnell O, Oden A, Johansson H, McCloskey E. FRAX and the assessment of fracture probability in men and women from the UK. *Osteoporos Int.* 2008; 19(4):385–97. [PubMed: 18292978]
13. Compston J. FRAX--Where are we now? *Maturitas.* 2015; 82(3):284–7. [PubMed: 26277257]
14. Bousson V, Bergot C, Sutter B, Levitz P, Cortet B. Trabecular bone score (TBS): available knowledge, clinical relevance, and future prospects. *Osteoporos Int.* 2012; 23(5):1489–501. [PubMed: 22083541]
15. Silva BC, Broy SB, Boutroy S, Schousboe JT, Shepherd JA, Leslie WD. Fracture Risk Prediction by Non-BMD DXA Measures: the 2015 ISCD Official Positions Part 2: Trabecular Bone Score. *Journal of clinical densitometry : the official journal of the International Society for Clinical Densitometry.* 2015; 18(3):309–30. [PubMed: 26277849]
16. Maquer G, Lu Y, Dall'Ara E, et al. The Initial Slope of the Variogram, Foundation of the Trabecular Bone Score, Is Not or Is Poorly Associated With Vertebral Strength. *J Bone Miner Res.* 2016; 31(2):341–6. [PubMed: 26234619]
17. Silva BC, Leslie WD, Resch H, et al. Trabecular bone score: a noninvasive analytical method based upon the DXA image. *J Bone Miner Res.* 2014; 29(3):518–30. [PubMed: 24443324]
18. Seeman E. Is a change in bone mineral density a sensitive and specific surrogate of anti-fracture efficacy? *Bone.* 2007; 41(3):308–17. [PubMed: 17644058]
19. Gartner, LP., Hiatt, JL., Gartner, LP. Color atlas and text of histology. 6. Philadelphia: Wolters Kluwer Health/Lippincott Williams & Wilkins; 2014.
20. Deyrup, AT., Siegal, GP. Practical orthopedic pathology : a diagnostic approach. Philadelphia, PA: Elsevier; 2016.
21. Dempster DW. Bone microarchitecture and strength. *Osteoporos Int.* 2003; 14(Suppl 5):S54–6. [PubMed: 14504707]

22. Kleerekoper M, Villanueva AR, Stanciu J, Rao DS, Parfitt AM. The role of three-dimensional trabecular microstructure in the pathogenesis of vertebral compression fractures. *Calcif Tissue Int.* 1985; 37(6):594–7. [PubMed: 3937580]
23. Amling M, Posl M, Ritzel H, et al. Architecture and distribution of cancellous bone yield vertebral fracture clues. A histomorphometric analysis of the complete spinal column from 40 autopsy specimens. *Arch Orthop Trauma Surg.* 1996; 115(5):262–9. [PubMed: 8836458]
24. Bala Y, Zebaze R, Seeman E. Role of cortical bone in bone fragility. *Curr Opin Rheumatol.* 2015; 27(4):406–13. [PubMed: 26002033]
25. Bala Y, Zebaze R, Ghasem-Zadeh A, et al. Cortical porosity identifies women with osteopenia at increased risk for forearm fractures. *J Bone Miner Res.* 2014; 29(6):1356–62. [PubMed: 24519558]
26. Ahmed LA, Shigdel R, Joakimsen RM, et al. Measurement of cortical porosity of the proximal femur improves identification of women with nonvertebral fragility fractures. *Osteoporos Int.* 2015; 26(8):2137–46. [PubMed: 25876879]
27. Link TM, Majumdar S, Augat P, et al. In vivo high resolution MRI of the calcaneus: differences in trabecular structure in osteoporosis patients. *J Bone Miner Res.* 1998; 13(7):1175–82. [PubMed: 9661082]
28. Majumdar S, Genant HK, Grampp S, et al. Correlation of trabecular bone structure with age, bone mineral density, and osteoporotic status: in vivo studies in the distal radius using high resolution magnetic resonance imaging. *J Bone Miner Res.* 1997; 12(1):111–8. [PubMed: 9240733]
29. Wehrli FW, Hwang SN, Ma J, Song HK, Ford JC, Haddad JG. Cancellous bone volume and structure in the forearm: noninvasive assessment with MR microimaging and image processing. *Radiology.* 1998; 206(2):347–57. [PubMed: 9457185]
30. Wehrli FW. Structural and functional assessment of trabecular and cortical bone by micro magnetic resonance imaging. *J Magn Reson Imaging.* 2007; 25(2):390–409. [PubMed: 17260403]
31. Haacke, EM. *Magnetic resonance imaging : physical principles and sequence design.* New York: Wiley; 1999.
32. Wright SM, Wald LL. Theory and application of array coils in MR spectroscopy. *NMR Biomed.* 1997; 10(8):394–410. [PubMed: 9542737]
33. Techawiboonwong A, Song HK, Magland JF, Saha PK, Wehrli FW. Implications of pulse sequence in structural imaging of trabecular bone. *J Magn Reson Imaging.* 2005; 22(5):647–55. [PubMed: 16215967]
34. Wehrli FW, Gomberg BR, Saha PK, Song HK, Hwang SN, Snyder PJ. Digital topological analysis of in vivo magnetic resonance microimages of trabecular bone reveals structural implications of osteoporosis. *J Bone Miner Res.* 2001; 16(8):1520–31. [PubMed: 11499875]
35. Krug R, Banerjee S, Han ET, Newitt DC, Link TM, Majumdar S. Feasibility of in vivo structural analysis of high-resolution magnetic resonance images of the proximal femur. *Osteoporos Int.* 2005; 16(11):1307–14. [PubMed: 15999292]
36. Carballido-Gamio J, Folkesson J, Karampinos DC, et al. Generation of an atlas of the proximal femur and its application to trabecular bone analysis. *Magn Reson Med.* 2011; 66(4):1181–91. [PubMed: 21432904]
37. Han M, Chiba K, Banerjee S, Carballido-Gamio J, Krug R. Variable flip angle three-dimensional fast spin-echo sequence combined with outer volume suppression for imaging trabecular bone structure of the proximal femur. *J Magn Reson Imaging.* 2014
38. Chang G, Deniz CM, Honig S, et al. Feasibility of three-dimensional MRI of proximal femur microarchitecture at 3 tesla using 26 receive elements without and with parallel imaging. *J Magn Reson Imaging.* 2014; 40(1):229–38. [PubMed: 24711013]
39. Chang G, Deniz CM, Honig S, et al. MRI of the hip at 7T: feasibility of bone microarchitecture, high-resolution cartilage, and clinical imaging. *J Magn Reson Imaging.* 2014; 39(6):1384–93. [PubMed: 24115554]
40. Chang G, Honig S, Brown R, et al. Finite Element Analysis Applied to 3-T MR Imaging of Proximal Femur Microarchitecture: Lower Bone Strength in Patients with Fragility Fractures Compared with Control Subjects. *Radiology.* 2014; 272(2):464–74. [PubMed: 24689884]

41. Banerjee S, Han ET, Krug R, Newitt DC, Majumdar S. Application of refocused steady-state free-precession methods at 1.5 and 3 T to in vivo high-resolution MRI of trabecular bone: simulations and experiments. *J Magn Reson Imaging*. 2005; 21(6):818–25. [PubMed: 15906346]
42. Cummings SR, Bates D, Black DM. Clinical use of bone densitometry: scientific review. *JAMA*. 2002; 288(15):1889–97. [PubMed: 12377088]
43. Cohen A, Dempster DW, Muller R, et al. Assessment of trabecular and cortical architecture and mechanical competence of bone by high-resolution peripheral computed tomography: comparison with transiliac bone biopsy. *Osteoporos Int*. 2010; 21(2):263–73. [PubMed: 19455271]
44. Liu XS, Cohen A, Shane E, et al. Bone density, geometry, microstructure, and stiffness: Relationships between peripheral and central skeletal sites assessed by DXA, HR-pQCT, and cQCT in premenopausal women. *J Bone Miner Res*. 2010; 25(10):2229–38. [PubMed: 20499344]
45. Eckstein F, Matsuura M, Kuhn V, et al. Sex differences of human trabecular bone microstructure in aging are site-dependent. *J Bone Miner Res*. 2007; 22(6):817–24. [PubMed: 17352643]
46. Carballido-Gamio J, Krug R, Huber MB, et al. Geodesic topological analysis of trabecular bone microarchitecture from high-spatial resolution magnetic resonance images. *Magn Reson Med*. 2009; 61(2):448–56. [PubMed: 19161163]
47. Saha PK, Gomberg BR, Wehrli FW. Three-dimensional digital topological characterization of cancellous bone architecture. *Int J Imaging Syst Technol*. 2000; 11:81–90.
48. Saha PK, Wehrli FW, Gomberg BR. Fuzzy distance transform: theory, algorithms, and applications. *Comput Vis Image Underst*. 2002; 86:171–90.
49. Rajapakse CS, Magland J, Zhang XH, et al. Implications of noise and resolution on mechanical properties of trabecular bone estimated by image-based finite-element analysis. *J Orthop Res*. 2009; 27(10):1263–71. [PubMed: 19338030]
50. Rajapakse CS, Magland JF, Wald MJ, et al. Computational biomechanics of the distal tibia from high-resolution MR and micro-CT images. *Bone*. 2010; 47(3):556–63. [PubMed: 20685323]
51. Liu XS, Zhang XH, Rajapakse CS, et al. Accuracy of high-resolution in vivo micro magnetic resonance imaging for measurements of microstructural and mechanical properties of human distal tibial bone. *J Bone Miner Res*. 2010; 25(9):2039–50. [PubMed: 20499379]
52. Newitt DC, Majumdar S, van Rietbergen B, et al. In vivo assessment of architecture and micro-finite element analysis derived indices of mechanical properties of trabecular bone in the radius. *Osteoporos Int*. 2002; 13(1):6–17. [PubMed: 11878456]
53. Zhang N, Magland JF, Rajapakse CS, Bhagat YA, Wehrli FW. Potential of in vivo MRI-based nonlinear finite-element analysis for the assessment of trabecular bone post-yield properties. *Med Phys*. 2013; 40(5):052303. [PubMed: 23635290]
54. Zhang N, Magland JF, Rajapakse CS, Lam SB, Wehrli FW. Assessment of trabecular bone yield and post-yield behavior from high-resolution MRI-based nonlinear finite element analysis at the distal radius of premenopausal and postmenopausal women susceptible to osteoporosis. *Acad Radiol*. 2013; 20(12):1584–91. [PubMed: 24200486]
55. Magland JF, Zhang N, Rajapakse CS, Wehrli FW. Computationally-optimized bone mechanical modeling from high-resolution structural images. *PloS one*. 2012; 7(4):e35525. [PubMed: 22558164]
56. Keaveny TM. Biomechanical computed tomography-noninvasive bone strength analysis using clinical computed tomography scans. *Ann N Y Acad Sci*. 2010; 1192:57–65. [PubMed: 20392218]
57. Keyak JH. Improved prediction of proximal femoral fracture load using nonlinear finite element models. *Med Eng Phys*. 2001; 23(3):165–73. [PubMed: 11410381]
58. Keyak JH, Kaneko TS, Rossi SA, Pejcic MR, Tehranzadeh J, Skinner HB. Predicting the strength of femoral shafts with and without metastatic lesions. *Clin Orthop Relat Res*. 2005; 439:161–70. [PubMed: 16205155]
59. Lang TF. Quantitative computed tomography. *Radiol Clin North Am*. 2010; 48(3):589–600. [PubMed: 20609894]
60. Cheung AM, Adachi JD, Hanley DA, et al. High-resolution peripheral quantitative computed tomography for the assessment of bone strength and structure: a review by the Canadian Bone Strength Working Group. *Current osteoporosis reports*. 2013; 11(2):136–46. [PubMed: 23525967]

61. Liu XS, Zhang XH, Sekhon KK, et al. High-resolution peripheral quantitative computed tomography can assess microstructural and mechanical properties of human distal tibial bone. *J Bone Miner Res.* 2010; 25(4):746–56. [PubMed: 19775199]
62. Nishiyama KK, Shane E. Clinical imaging of bone microarchitecture with HR-pQCT. *Current osteoporosis reports.* 2013; 11(2):147–55. [PubMed: 23504496]
63. Melton LJ 3rd, Riggs BL, van Lenthe GH, et al. Contribution of in vivo structural measurements and load/strength ratios to the determination of forearm fracture risk in postmenopausal women. *J Bone Miner Res.* 2007; 22(9):1442–8. [PubMed: 17539738]
64. Horch RA, Nyman JS, Gochberg DF, Dortch RD, Does MD. Characterization of ¹H NMR signal in human cortical bone for magnetic resonance imaging. *Magn Reson Med.* 2010; 64(3):680–7. [PubMed: 20806375]
65. Ma YJ, Chang EY, Bydder GM, Du J. Can ultrashort-TE (UTE) MRI sequences on a 3-T clinical scanner detect signal directly from collagen protons: freeze-dry and D₂O exchange studies of cortical bone and Achilles tendon specimens. *NMR Biomed.* 2016; 29(7):912–7. [PubMed: 27148693]
66. Du J, Bydder GM. Qualitative and quantitative ultrashort-TE MRI of cortical bone. *NMR Biomed.* 2013; 26(5):489–506. [PubMed: 23280581]
67. Seifert AC, Wehrli FW. Solid-State Quantitative (¹H and (³¹P MRI of Cortical Bone in Humans. *Current osteoporosis reports.* 2016; 14(3):77–86. [PubMed: 27048472]
68. Chang EY, Du J, Chung CB. UTE imaging in the musculoskeletal system. *J Magn Reson Imaging.* 2015; 41(4):870–83. [PubMed: 25045018]
69. Techawiboonwong A, Song HK, Leonard MB, Wehrli FW. Cortical bone water: in vivo quantification with ultrashort echo-time MR imaging. *Radiology.* 2008; 248(3):824–33. [PubMed: 18632530]
70. Manhard MK, Horch RA, Gochberg DF, Nyman JS, Does MD. In Vivo Quantitative MR Imaging of Bound and Pore Water in Cortical Bone. *Radiology.* 2015; 277(1):221–9. [PubMed: 26020434]
71. Chen J, Carl M, Ma Y, et al. Fast volumetric imaging of bound and pore water in cortical bone using three-dimensional ultrashort-TE (UTE) and inversion recovery UTE sequences. *NMR Biomed.* 2016
72. Li C, Seifert AC, Rad HS, et al. Cortical bone water concentration: dependence of MR imaging measures on age and pore volume fraction. *Radiology.* 2014; 272(3):796–806. [PubMed: 24814179]
73. Rajapakse CS, Bashoor-Zadeh M, Li C, Sun W, Wright AC, Wehrli FW. Volumetric Cortical Bone Porosity Assessment with MR Imaging: Validation and Clinical Feasibility. *Radiology.* 2015; 276(2):526–35. [PubMed: 26203710]
74. Chiang JT, Carl M, Du J. Signal and contrast effects due to T₂ decay during k-space readout of UTE (ultrashort TE) sequences. *Magn Reson Imaging.* 2014; 32(3):259–69. [PubMed: 24457160]
75. Weiger M, Pruessmann KP, Hennel F. MRI with zero echo time: hard versus sweep pulse excitation. *Magn Reson Med.* 2011; 66(2):379–89. [PubMed: 21381099]
76. Ackerman JL, Raleigh DP, Glimcher MJ. Phosphorus-31 magnetic resonance imaging of hydroxyapatite: a model for bone imaging. *Magn Reson Med.* 1992; 25(1):1–11. [PubMed: 1317501]
77. Idiyatullin D, Corum C, Park JY, Garwood M. Fast and quiet MRI using a swept radiofrequency. *J Magn Reson.* 2006; 181(2):342–9. [PubMed: 16782371]
78. Idiyatullin D, Corum CA, Nixdorf DR, Garwood M. Intraoral approach for imaging teeth using the transverse B₁ field components of an occlusally oriented loop coil. *Magn Reson Med.* 2014; 72(1):160–5. [PubMed: 23900995]
79. Seifert AC, Li C, Rajapakse CS, et al. Bone mineral (³¹P and matrix-bound water densities measured by solid-state (³¹P and (¹H MRI. *NMR Biomed.* 2014; 27(7):739–48. [PubMed: 24846186]
80. Wu Y, Reese TG, Cao H, et al. Bone mineral imaged in vivo by ³¹P solid state MRI of human wrists. *J Magn Reson Imaging.* 2011; 34(3):623–33. [PubMed: 21761459]
81. Robson MD, Gatehouse PD, Bydder GM, Neubauer S. Human imaging of phosphorus in cortical and trabecular bone in vivo. *Magn Reson Med.* 2004; 51(5):888–92. [PubMed: 15122669]

82. Gee CS, Nguyen JT, Marquez CJ, et al. Validation of bone marrow fat quantification in the presence of trabecular bone using MRI. *J Magn Reson Imaging*. 2015; 42(2):539–44. [PubMed: 25425074]
83. Di Pietro G, Capuani S, Manenti G, et al. Bone Marrow Lipid Profiles from Peripheral Skeleton as Potential Biomarkers for Osteoporosis: A 1H-MR Spectroscopy Study. *Acad Radiol*. 2016; 23(3): 273–83. [PubMed: 26774740]
84. Pansini V, Monnet A, Salleron J, Hardouin P, Cortet B, Cotten A. 3 Tesla (1) H MR spectroscopy of hip bone marrow in a healthy population, assessment of normal fat content values and influence of age and sex. *J Magn Reson Imaging*. 2014; 39(2):369–76. [PubMed: 23677563]
85. Yeung DK, Griffith JF, Antonio GE, Lee FK, Woo J, Leung PC. Osteoporosis is associated with increased marrow fat content and decreased marrow fat unsaturation: a proton MR spectroscopy study. *J Magn Reson Imaging*. 2005; 22(2):279–85. [PubMed: 16028245]
86. Patsch JM, Li X, Baum T, et al. Bone marrow fat composition as a novel imaging biomarker in postmenopausal women with prevalent fragility fractures. *J Bone Miner Res*. 2013
87. Karampinos DC, Melkus G, Baum T, Bauer JS, Rummeny EJ, Krug R. Bone marrow fat quantification in the presence of trabecular bone: initial comparison between water-fat imaging and single-voxel MRS. *Magn Reson Med*. 2014; 71(3):1158–65. [PubMed: 23657998]
88. Cordes C, Baum T, Dieckmeyer M, et al. MR-Based Assessment of Bone Marrow Fat in Osteoporosis, Diabetes, and Obesity. *Front Endocrinol (Lausanne)*. 2016; 7:74. [PubMed: 27445977]
89. Li G, Xu Z, Gu H, et al. Comparison of chemical shift-encoded water-fat MRI and MR spectroscopy in quantification of marrow fat in postmenopausal females. *J Magn Reson Imaging*. 2016
90. Ojanen X, Borra RJ, Havu M, et al. Comparison of vertebral bone marrow fat assessed by 1H MRS and inphase and out-of-phase MRI among family members. *Osteoporos Int*. 2014; 25(2):653–62. [PubMed: 23943163]
91. Kuhn JP, Hernando D, Meffert PJ, et al. Proton-density fat fraction and simultaneous R2* estimation as an MRI tool for assessment of osteoporosis. *Eur Radiol*. 2013; 23(12):3432–9. [PubMed: 23812246]
92. Li X, Kuo D, Schafer AL, et al. Quantification of vertebral bone marrow fat content using 3 Tesla MR spectroscopy: reproducibility, vertebral variation, and applications in osteoporosis. *J Magn Reson Imaging*. 2011; 33(4):974–9. [PubMed: 21448966]
93. Schwartz AV. Marrow fat and bone: review of clinical findings. *Front Endocrinol (Lausanne)*. 2015; 6:40. [PubMed: 25870585]
94. Ma HT, Griffith JF, Zhao X, Lv H, Yeung DK, Leung PC. Relationship between marrow perfusion and bone mineral density: a pharmacokinetic study of DCE-MRI. *Conf Proc IEEE Eng Med Biol Soc*. 2012; 2012:377–9. [PubMed: 23365908]
95. Ma HT, Lv H, Griffith JF, Yuan J, Leung PC. Bone marrow perfusion of proximal femur varied with BMD--a longitudinal study by DCE-MRI. *Conf Proc IEEE Eng Med Biol Soc*. 2013; 2013:2607–10. [PubMed: 24110261]
96. Budzik JF, Lefebvre G, Forzy G, El Rafei M, Chechin D, Cotten A. Study of proximal femoral bone perfusion with 3D T1 dynamic contrast-enhanced MRI: a feasibility study. *Eur Radiol*. 2014; 24(12):3217–23. [PubMed: 25120203]
97. Dyke JP, Lazaro LE, Hettrich CM, Hentel KD, Helfet DL, Lorich DG. Regional analysis of femoral head perfusion following displaced fractures of the femoral neck. *J Magn Reson Imaging*. 2015; 41(2):550–4. [PubMed: 24338938]
98. Biffar A, Schmidt GP, Sourbron S, et al. Quantitative analysis of vertebral bone marrow perfusion using dynamic contrast-enhanced MRI: initial results in osteoporotic patients with acute vertebral fracture. *J Magn Reson Imaging*. 2011; 33(3):676–83. [PubMed: 21563252]
99. Griffith JF, Yeung DK, Leung JC, Kwok TC, Leung PC. Prediction of bone loss in elderly female subjects by MR perfusion imaging and spectroscopy. *Eur Radiol*. 2011; 21(6):1160–9. [PubMed: 21225266]

100. Wang YX, Griffith JF, Kwok AW, et al. Reduced bone perfusion in proximal femur of subjects with decreased bone mineral density preferentially affects the femoral neck. *Bone*. 2009; 45(4): 711–5. [PubMed: 19555783]
101. Griffith JF, Yeung DK, Tsang PH, et al. Compromised bone marrow perfusion in osteoporosis. *J Bone Miner Res*. 2008; 23(7):1068–75. [PubMed: 18302498]
102. Ohno N, Miyati T, Kasai H, et al. Evaluation of perfusion-related and true diffusion in vertebral bone marrow: a preliminary study. *Radiol Phys Technol*. 2015; 8(1):135–40. [PubMed: 25413477]
103. Marchand AJ, Hitti E, Monge F, et al. MRI quantification of diffusion and perfusion in bone marrow by intravoxel incoherent motion (IVIM) and non-negative least square (NNLS) analysis. *Magn Reson Imaging*. 2014; 32(9):1091–6. [PubMed: 25093628]
104. Griffith JF, Yeung DK, Antonio GE, et al. Vertebral marrow fat content and diffusion and perfusion indexes in women with varying bone density: MR evaluation. *Radiology*. 2006; 241(3): 831–8. [PubMed: 17053202]
105. Manenti G, Capuani S, Fanucci E, et al. Diffusion tensor imaging and magnetic resonance spectroscopy assessment of cancellous bone quality in femoral neck of healthy, osteopenic and osteoporotic subjects at 3T: Preliminary experience. *Bone*. 2013; 55(1):7–15. [PubMed: 23507402]
106. Rebuzzi M, Vinicola V, Taggi F, Sabatini U, Wehrli FW, Capuani S. Potential diagnostic role of the MRI-derived internal magnetic field gradient in calcaneus cancellous bone for evaluating postmenopausal osteoporosis at 3T. *Bone*. 2013; 57(1):155–63. [PubMed: 23899635]
107. Sprinkhuizen SM, Ackerman JL, Song YQ. Influence of bone marrow composition on measurements of trabecular microstructure using decay due to diffusion in the internal field MRI: simulations and clinical studies. *Magn Reson Med*. 2014; 72(6):1499–508. [PubMed: 24382681]
108. Sung JK, Jee WH, Jung JY, et al. Differentiation of acute osteoporotic and malignant compression fractures of the spine: use of additive qualitative and quantitative axial diffusion-weighted MR imaging to conventional MR imaging at 3.0 T. *Radiology*. 2014; 271(2):488–98. [PubMed: 24484060]
109. Frost ML, Moore AE, Siddique M, et al. (1)(8)F-fluoride PET as a noninvasive imaging biomarker for determining treatment efficacy of bone active agents at the hip: a prospective, randomized, controlled clinical study. *J Bone Miner Res*. 2013; 28(6):1337–47. [PubMed: 23322666]
110. Blake GM, Siddique M, Frost ML, Moore AE, Fogelman I. Imaging of site specific bone turnover in osteoporosis using positron emission tomography. *Current osteoporosis reports*. 2014; 12(4): 475–85. [PubMed: 25168931]
111. Al-Beyatti Y, Siddique M, Frost ML, Fogelman I, Blake GM. Precision of (1)(8)F-fluoride PET skeletal kinetic studies in the assessment of bone metabolism. *Osteoporos Int*. 2012; 23(10): 2535–41. [PubMed: 22237817]
112. Frost ML, Siddique M, Blake GM, et al. Regional bone metabolism at the lumbar spine and hip following discontinuation of alendronate and risedronate treatment in postmenopausal women. *Osteoporos Int*. 2012; 23(8):2107–16. [PubMed: 21983795]
113. Newitt DC, van Rietbergen B, Majumdar S. Processing and analysis of in vivo high-resolution MR images of trabecular bone for longitudinal studies: reproducibility of structural measures and micro-finite element analysis derived mechanical properties. *Osteoporos Int*. 2002; 13(4):278–87. [PubMed: 12030542]
114. Gomberg BR, Wehrli FW, Vasilic B, et al. Reproducibility and error sources of micro-MRI-based trabecular bone structural parameters of the distal radius and tibia. *Bone*. 2004; 35(1):266–76. [PubMed: 15207767]
115. Lam SC, Wald MJ, Rajapakse CS, Liu Y, Saha PK, Wehrli FW. Performance of the MRI-based virtual bone biopsy in the distal radius: serial reproducibility and reliability of structural and mechanical parameters in women representative of osteoporosis study populations. *Bone*. 2011; 49(4):895–903. [PubMed: 21784189]

116. Wald MJ, Magland JF, Rajapakse CS, Wehrli FW. Structural and mechanical parameters of trabecular bone estimated from in vivo high-resolution magnetic resonance images at 3 tesla field strength. *J Magn Reson Imaging*. 2010; 31(5):1157–68. [PubMed: 20432352]
117. Zuo J, Bolbos R, Hammond K, Li X, Majumdar S. Reproducibility of the quantitative assessment of cartilage morphology and trabecular bone structure with magnetic resonance imaging at 7 T. *Magn Reson Imaging*. 2008; 26(4):560–6. [PubMed: 18060717]
118. Bhagat YA, Rajapakse CS, Magland JF, et al. Performance of muMRI-Based virtual bone biopsy for structural and mechanical analysis at the distal tibia at 7T field strength. *J Magn Reson Imaging*. 2011; 33(2):372–81. [PubMed: 21274979]
119. Chang G, Hotca-Cho A, Rusinek H, et al. Measurement reproducibility of magnetic resonance imaging-based finite element analysis of proximal femur microarchitecture for in vivo assessment of bone strength. *MAGMA*. 2015; 28(4):407–12. [PubMed: 25487834]
120. Hotca A, Rajapakse CS, Cheng C, et al. In vivo measurement reproducibility of femoral neck microarchitectural parameters derived from 3T MR images. *J Magn Reson Imaging*. 2015
121. Rajapakse CS, Honig S, Ramme A, et al. Patient Specific Hip Fracture Strength Assessment by Microstructural MRI Based Finite Element Modeling. *Radiology*. In Press.
122. Kijowski R, Tuite M, Kruger D, Munoz Del Rio A, Kleerekoper M, Binkley N. Evaluation of trabecular microarchitecture in nonosteoporotic postmenopausal women with and without fracture. *J Bone Miner Res*. 2012; 27(7):1494–500. [PubMed: 22407970]
123. Chang G, Honig S, Liu Y, et al. 7 Tesla MRI of bone microarchitecture discriminates between women without and with fragility fractures who do not differ by bone mineral density. *J Bone Miner Metab*. 2014
124. Ladinsky GA, Vasilic B, Popescu AM, et al. Trabecular structure quantified with the MRI-based virtual bone biopsy in postmenopausal women contributes to vertebral deformity burden independent of areal vertebral BMD. *J Bone Miner Res*. 2008; 23(1):64–74. [PubMed: 17784842]
125. Rajapakse CS, Phillips EA, Sun W, et al. Vertebral deformities and fractures are associated with MRI and pQCT measures obtained at the distal tibia and radius of postmenopausal women. *Osteoporos Int*. 2014; 25(3):973–82. [PubMed: 24221453]
126. Greenspan SL, Wagner J, Nelson JB, Perera S, Britton C, Resnick NM. Vertebral fractures and trabecular microstructure in men with prostate cancer on androgen deprivation therapy. *J Bone Miner Res*. 2013; 28(2):325–32. [PubMed: 22991066]
127. van Staa TP, Leufkens HG, Cooper C. The epidemiology of corticosteroid-induced osteoporosis: a meta-analysis. *Osteoporos Int*. 2002; 13(10):777–87. [PubMed: 12378366]
128. Kanis JA, Johansson H, Oden A, et al. A meta-analysis of prior corticosteroid use and fracture risk. *J Bone Miner Res*. 2004; 19(6):893–9. [PubMed: 15125788]
129. Chang G, Rajapakse CS, Regatte RR, et al. 3 Tesla MRI detects deterioration in proximal femur microarchitecture and strength in long-term glucocorticoid users compared with controls. *J Magn Reson Imaging*. 2015
130. Rajapakse CS, Leonard MB, Bhagat YA, Sun W, Magland JF, Wehrli FW. Micro-MR Imaging-based Computational Biomechanics Demonstrates Reduction in Cortical and Trabecular Bone Strength after Renal Transplantation. *Radiology*. 2012; 262:921–31. [PubMed: 22267587]
131. Starup-Linde J, Frost M, Vestergaard P, Abrahamsen B. Epidemiology of Fractures in Diabetes. *Calcif Tissue Int*. 2016
132. Sellmeyer DE, Civitelli R, Hofbauer LC, Khosla S, Lecka-Czernik B, Schwartz AV. Skeletal Metabolism, Fracture Risk, and Fracture Outcomes in Type 1 and Type 2 Diabetes. *Diabetes*. 2016; 65(7):1757–66. [PubMed: 27329951]
133. Abdalrahman N, McComb C, Foster JE, et al. Deficits in Trabecular Bone Microarchitecture in Young Women With Type 1 Diabetes Mellitus. *J Bone Miner Res*. 2015; 30(8):1386–93. [PubMed: 25627460]
134. Pritchard JM, Giangregorio LM, Atkinson SA, et al. Association of larger holes in the trabecular bone at the distal radius in postmenopausal women with type 2 diabetes mellitus compared to controls. *Arthritis Care Res (Hoboken)*. 2012; 64(1):83–91. [PubMed: 22213724]

135. Pritchard JM, Giangregorio LM, Atkinson SA, et al. Changes in trabecular bone microarchitecture in postmenopausal women with and without type 2 diabetes: a two year longitudinal study. *BMC musculoskeletal disorders*. 2013; 14:114. [PubMed: 23530948]
136. Modlesky CM, Subramanian P, Miller F. Underdeveloped trabecular bone microarchitecture is detected in children with cerebral palsy using high-resolution magnetic resonance imaging. *Osteoporos Int*. 2008; 19(2):169–76. [PubMed: 17962918]
137. Modlesky CM, Whitney DG, Singh H, Barbe MF, Kirby JT, Miller F. Underdevelopment of trabecular bone microarchitecture in the distal femur of nonambulatory children with cerebral palsy becomes more pronounced with distance from the growth plate. *Osteoporos Int*. 2015; 26(2):505–12. [PubMed: 25199575]
138. Greenspan SL, Perera S, Recker R, et al. Changes in trabecular microarchitecture in postmenopausal women on bisphosphonate therapy. *Bone*. 2010; 46(4):1006–10. [PubMed: 20051275]
139. Folkesson J, Goldenstein J, Carballido-Gamio J, et al. Longitudinal evaluation of the effects of alendronate on MRI bone microarchitecture in postmenopausal osteopenic women. *Bone*. 2011; 48(3):611–21. [PubMed: 21059422]
140. Black DM, Bouxsein ML, Palermo L, et al. Randomized trial of once-weekly parathyroid hormone (1–84) on bone mineral density and remodeling. *J Clin Endocrinol Metab*. 2008; 93(6): 2166–72. [PubMed: 18349061]
141. Wehrli FW, Ladinsky GA, Jones C, et al. In vivo magnetic resonance detects rapid remodeling changes in the topology of the trabecular bone network after menopause and the protective effect of estradiol. *J Bone Miner Res*. 2008; 23(5):730–40. [PubMed: 18251704]
142. Zhang XH, Liu XS, Vasilic B, et al. In vivo microMRI-based finite element and morphological analyses of tibial trabecular bone in eugonadal and hypogonadal men before and after testosterone treatment. *J Bone Miner Res*. 2008; 23(9):1426–34. [PubMed: 18410234]
143. Gordon KE, Wald MJ, Schnitzer TJ. Effect of parathyroid hormone combined with gait training on bone density and bone architecture in people with chronic spinal cord injury. *PM R*. 2013; 5(8):663–71. [PubMed: 23558091]

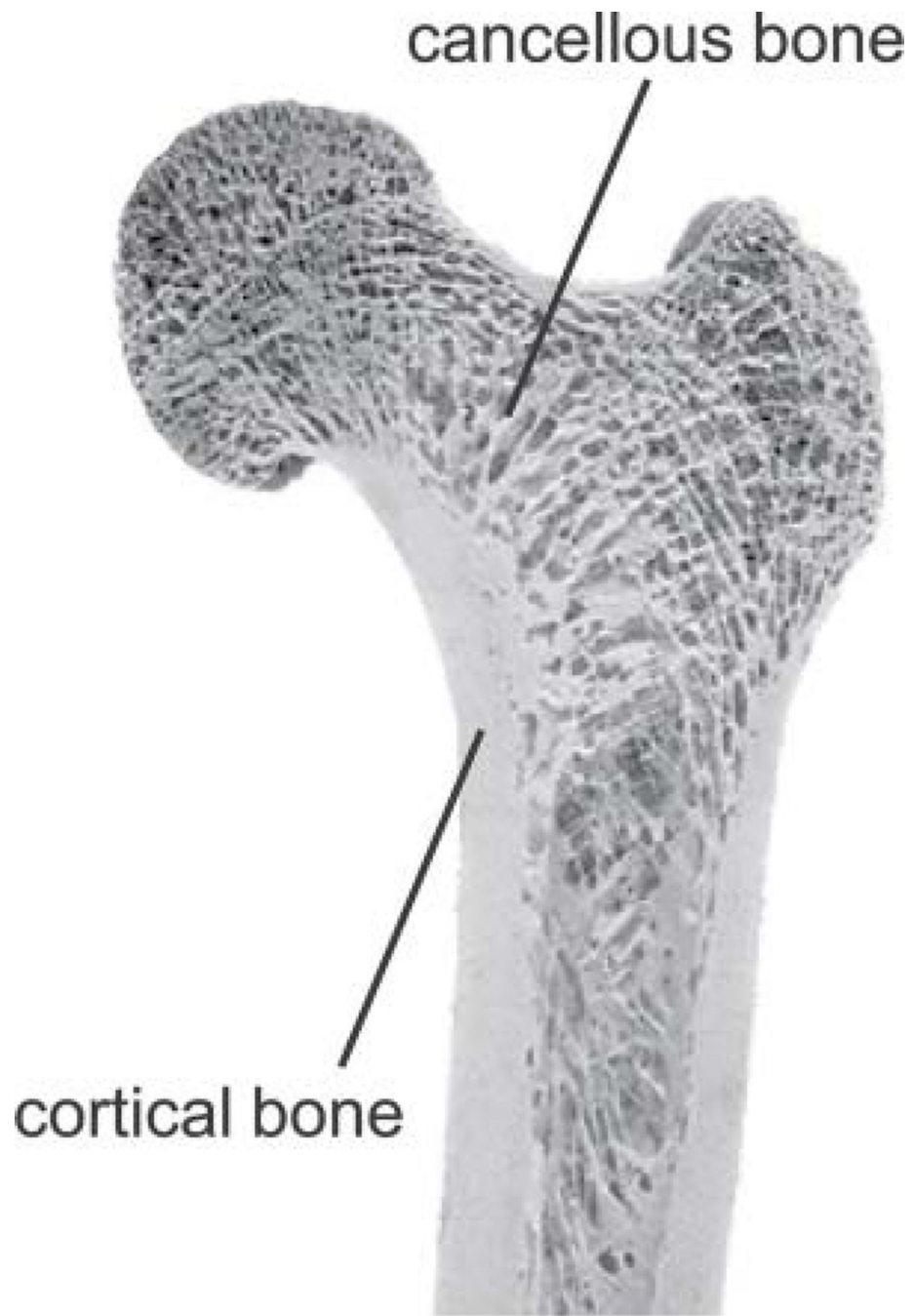


Figure 1.

Proximal femur specimen showing that bone tissue is composed of an outer, denser shell of cortical bone and an internal compartment of trabecular or cancellous bone. Reprinted with permission from Willems N et al. *European Journal of Orthodontics* 2014; 36:479–485.

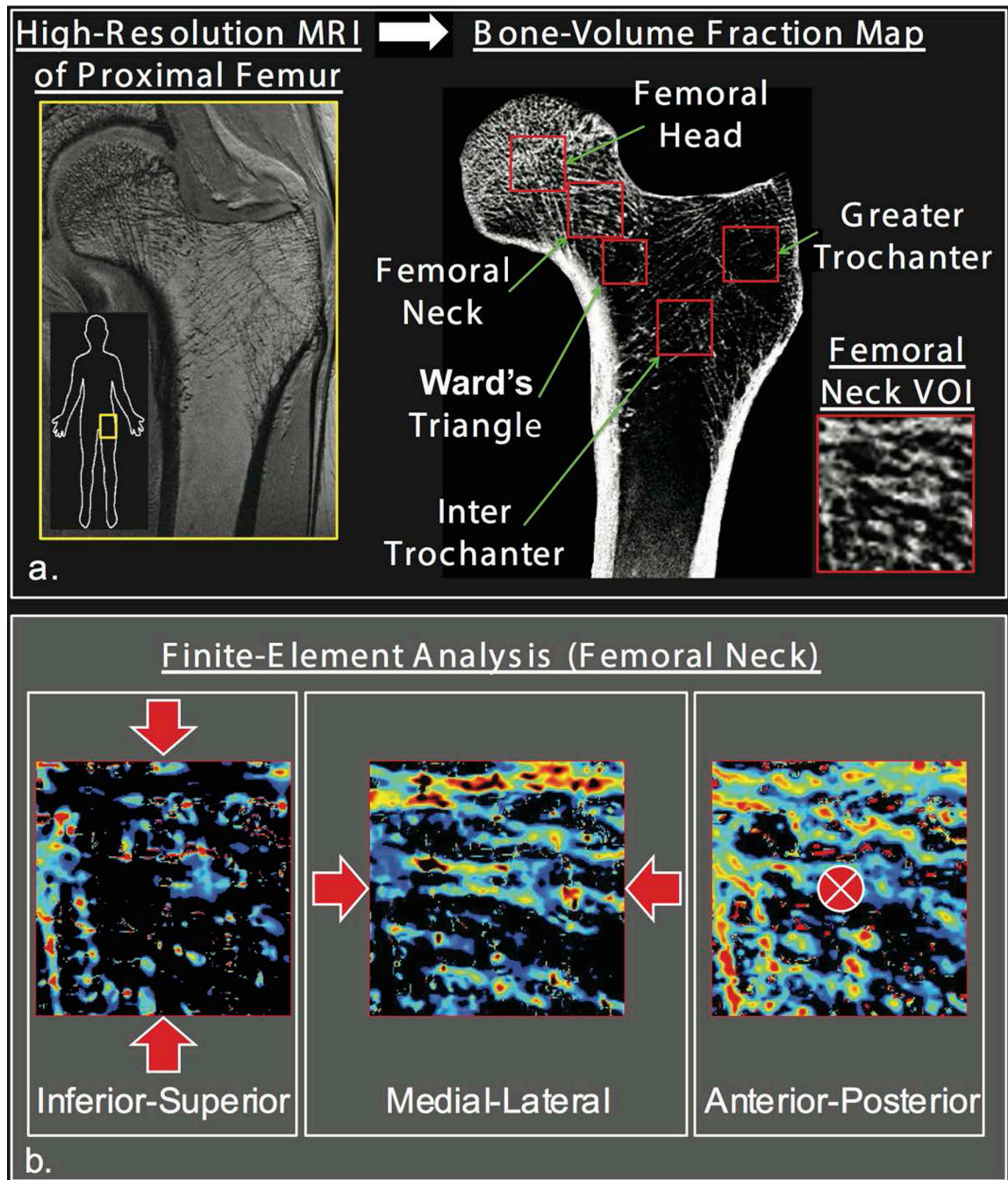


Figure 2.

Finite element analysis (FEA) allows in vivo estimation of bone mechanical properties. FEA was recently applied to in vivo 3T MR images of hip microarchitecture with simulated loading (three axes) applied to cubic volumes of interest to compute elastic modulus of trabecular bone in different proximal femur regions. Reprinted with permission from Chang et al. *Radiology* 2014; 272: 464–474.

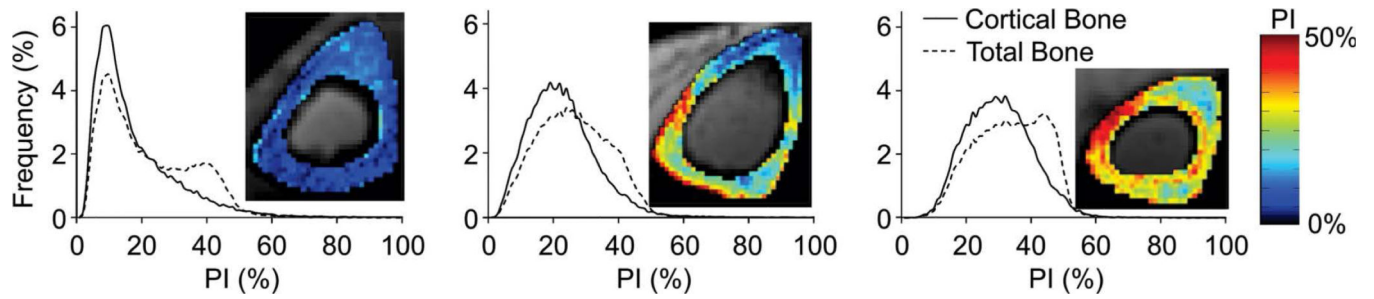


Figure 3.

UTE MRI can be used to compute a volumetric cortical bone porosity index by obtaining the ratio of signal intensities at long and short echo times. Representative volumetric cortical porosity index maps from three postmenopausal women obtained in vivo at the mid-tibia show a range of cortical porosities. Reprinted with permission from Rajapakse et al. *Radiology* 2015; 276:526–535.



Figure 4.

3T MRI reveals deterioration in proximal femur bone microarchitecture in a fragility fracture subject (left panel) compared to a control subject (right panel). In one study, when FEA was applied to subregional volumes of interest in the proximal femur, there was decreased elastic modulus in fragility fracture subjects compared to controls in all subregions analyzed (femoral head, neck, greater trochanter, intertrochanteric region). Reprinted with permission from Chang et al. *Radiology* 2014; 272:464–474.

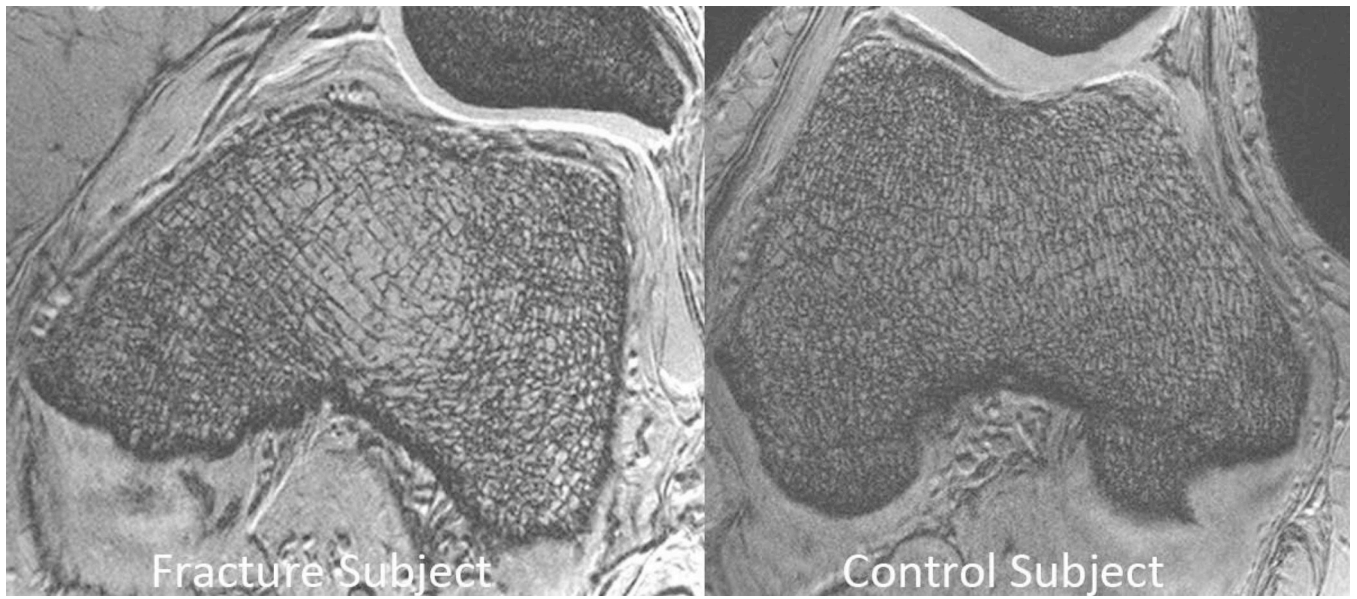


Figure 5.

7T MRI reveals deterioration in distal femur trabecular bone microarchitecture in a fragility fracture subject (left panel) compared to a control subject (right panel). The fracture subject demonstrates fewer trabeculae, which are disconnected, and more widely spaced apart.

Table 1

Table summarizing applications and techniques available for assessment of bone microarchitecture and structure.

Application	Technique
Assessment of Cortical Bone Total Water	UTE-MRI(69)
Assessment of Cortical Bound and Pore Water	UTE with Biexponential Analysis (71)
Assessment of Cortical Pore Water	UTE double adiabatic full passage(70), UTE Suppression Ratio (72), UTE Porosity Index (73)
Assessment of Cortical Bound Water	UTE adiabatic inversion recovery (70), UTE inversion recovery (71)
Assessment of Trabecular Bone Microarchitecture for Discriminating Fracture Cases from Controls or Monitoring Longitudinal Changes	3-D FLASE (30), 3-D FLASH (40), 3-D bSSFP (139), 3-D FSE (37)

Author Manuscript

Author Manuscript

Author Manuscript

Author Manuscript